Improved curved-boundary scheme for lattice Boltzmann simulation of microscale gas flow with second-order slip condition

Wentao Dai, Huiying Wu [*], Zhenyu Liu, and Shengyuan Zhang
School of Mechanical Engineering, Shanghai Jiao Tong University, Shanghai 200240 China

An improved curved-boundary scheme with second-order velocity slip condition for multiple-relaxation-time–lattice Boltzmann (MRT-LB) simulation of microgas flow is proposed. The proposed interpolation bounce-back (IBB)–explicit counter-extrapolation (ECE) scheme adopts the IBB method to describe the curved boundary, while the ECE method is employed to predict the slip velocity on gas-solid interface. To incorporate the effect of second-order velocity slip term and the influence of boundary curvature, a slip velocity model is also derived, from which the gas slip velocity is captured by the ECE discretization method. The influence of fictitious slip velocity can be eliminated by adopting the present ECE method, and the influence of actual offset between the lattice node and the physical boundary can be well considered by the IBB method. The proposed IBB-ECE boundary scheme is then implemented with the MRT-LB model and tested by simulations of force-driven gas flow in horizontal (inclined) microchannel, gas flow around a micro-cylinder, and Couette flow between two micro-cylinders. Numerical results show that the proposed IBB-ECE scheme improves the computational accuracy of gas slip flow $(0.001 < \text{Kn} \leqslant 0.1)$ when compared with other boundary schemes reported in the literature, and provides a precise and easy implementing scheme for curved boundary with second-order slip condition.

I. INTRODUCTION

The micro-gas flow has attracted increasing attention over the past few years due to its important applications in micronozzle, micro-combustor, micro-gas sensor, porous media, microfiber, etc. [1–7]. In these innovative applications, the Knudsen number ($\text{Kn} = \lambda/L$, which is defined as the ratio of the mean-free path of gas λ to the characteristic size of system L) is usually used to describe the microscale effect. Generally, the continuum assumption is no longer valid for micro-gas flow as $\text{Kn} > 0.001$ [8], and the traditional computational fluid dynamics approach based on the continuum assumption becomes less efficient for gas flow in slip regime as $0.001 < \text{Kn} \leqslant 0.1$ [9,10]. The lattice Boltzmann (LB) method derived from the Boltzmann equation, however, has been considered as an effective numerical approach for gas slip flow due to its kinetic origin and natural parallelism [11–13]. At present, the LB method has been successfully used in the simulation of gas slip flow with straight boundaries, and many second-order velocity slip schemes have been developed for straight boundaries [14–20]. However, the related researches for curved boundaries are relatively limited.

Szalmás [21] combined the specular-reflection bounce-back (SRB) boundary scheme and the body-fitted curvilinear coordinate system for the LB simulating of gas slip flow with curved boundary. However, the body-fitted mesh can only be used for the computational domain with a simple geometry and it greatly increases the complexity of programming.

The boundary scheme in the Cartesian coordinate system can avoid the disadvantages of the body-fitted coordinate system, and thus has attracted more attention. For instance, Augusto *et al.* [22] adopted the specular-reflection scheme with Cartesian uniform grids to realize a free-slip boundary condition for microfibers, and achieved a good accuracy for flow within an inclined microchannel and flow over an octagon. Guo *et al.* [23] applied the halfway diffusive-bounce-back (DBB) scheme in the simulation of micro-gas flow between two cylindrical surfaces. The curved surfaces were simplified as zigzag lines in their work, leading to a deterioration of simulation accuracy. It should also be pointed out that although the halfway DBB scheme has superiority in locality and could ensure the second-order slip boundary condition with a straight wall, the influence of boundary curvature cannot be considered by this scheme [24], which would induce deviations when used for a curved boundary. Suga [25] combined the DBB scheme with the interpolation method to simulate the micro-gas flow over a triangular cylinder. Although the boundary was described by the interpolation method, the combination parameters and the relaxation times were still chosen as the same as the halfway DBB scheme, which leads to numerical deviations [26]. To achieve the second-order slip condition with curved boundary, Tao and Guo [27] considered the offset between lattice nodes and curved boundary into the DBB scheme and modified the combination parameters and relaxation times of the multiple-relaxation-time–lattice Boltzmann (MRT-LB) model. This modified DBB scheme inherited the advantages of the halfway DBB scheme, making it possible to capture the second-order velocity slip and remain a good locality at the same time. However, the derivations of

*whysrj@sjtu.edu.cn

combination coefficients and relaxation times are based on the assumption of Poiseuille flow with a straight boundary, which still neglected the influence of the boundary curvature [20], leading to the decrease of simulation accuracy. In general, the above-mentioned slip curved-boundary schemes based on the kinetic theory have advantage in locality, but it is difficult to ensure the second-order slip condition for curved boundaries due to the difficulties of determining combination parameters and relaxation times and the neglection of the influence of boundary curvature.

In order to avoid the above disadvantages and massive derivations from kinetic theory, some researchers tried to discretize existing slip boundary models directly. This direct discretization method avoids the risk of inappropriate assumptions during derivation, involves no specific gas-solid interaction parameters, and could ensure a good accuracy if an appropriate slip model were selected. Tian *et al.* [28] discretized the Maxwell first-order slip model for gas slip flow in straight microchannels using the implicit extrapolation method, but this scheme is not capable of simulating flows with curved boundary and is only of first-order slip condition. To improve the simulation accuracy, Chen and Tian [29] discretized the Langmuir slip model for the gas slip flow and obtained good results, while the method is also only applicable for a straight boundary. Silva *et al.* [30,31] modified the multireflection scheme and proposed linear and parabolic slip velocity schemes for both straight and curved boundaries. Their schemes could maintain the second-order slip condition for a straight boundary but reduced to the first-order slip condition for a curved boundary. Recently, Liu *et al.* [32] proposed an improved curved-boundary scheme to consider the influence of boundary curvature. By combining the nonequilibrium extrapolation (NEE) method for curved wall and the counter-extrapolation (CE) method [33] for discretization, the Maxwell first-order velocity slip condition was precisely simulated. Nevertheless, the ignorance of the second-order slip term led to deviation when the Kn number became larger. Moreover, the implicit extrapolation was adopted for discretization and the choice of relaxation times was not provided in Liu *et al.*'s work [29], both of which would introduce a fictitious slip velocity along the curved boundary and lead to a deterioration of numerical accuracy [34]. Generally, the above slip curved-boundary schemes based on direct discretization method are simple in implementation, and are capable of simulating the influence of boundary curvature, while few related works considering the second-order slip effect have been reported in the literature.

As reviewed above, the curved slip boundary schemes based on kinetic theory have difficulty in considering the influence of boundary curvature and ensuring the second-order slip condition for a curved boundary, while the existing schemes based on direct discretization method can only simulate the first-order slip condition. To achieve an accurate and easy-implementing slip boundary scheme for a curved boundary, an improved curved boundary scheme with second-order slip condition based on direct discretization will be proposed in this work. In this scheme, a slip velocity model is derived by considering the influences of both the second-order velocity slip term and the boundary curvature radius, and the slip

effect is captured by discretizing the second-order slip velocity model through the explicit counter-extrapolation (ECE) method and bilinear interpolation method directly. Combined with the interpolation bounce-back (IBB) [35], the scheme is able to describe the curved boundary precisely, and the fictitious slip velocity induced by the IBB method can be eliminated by adopting the explicit CE method. The remainder of the present paper is organized as follows. Section II presents the adopted MRT-LB model for micro-gas flow. Section III introduces the derivation and implementation of the present second-order slip curved-boundary scheme. The validation tests of the proposed scheme are carried out in Sec. IV. Finally, a brief conclusion is drawn in Sec. V.

II. LATTICE BOLTZMANN MODEL FOR MICROGAS FLOW

The LB method has been proven as a powerful approach for simulation of microscale gas flow [36]. Considering that the lattice Bhatnagar-Gross-Krook model would produce a fictitious slip velocity between the wall and the fluid [37], the MRT-LB model [38] is adopted in the present work, and the evolution equation for the density distribution function can be expressed in a vector form as

$$\mathbf{f}(\mathbf{x} + \mathbf{c}\delta_t, t + \delta_t) - \mathbf{f}(\mathbf{x}, t) = -\mathbf{M}^{-1}\mathbf{S}[\mathbf{m} - \mathbf{m}^{\mathbf{eq}}] + \delta_t \mathbf{M}^{-1}\mathbf{F_m},$$
(1)

where $\mathbf{c}$ is the discrete velocity, δ_t is the time step; $\mathbf{M}$ and $\mathbf{S}$ are the transformation matrix and relaxation matrix, respectively; $\mathbf{m} = \mathbf{M}\mathbf{f}$ and $\mathbf{m}^{\mathbf{eq}} = \mathbf{M}\mathbf{f}^{\mathbf{eq}}$ are the projections of the density distribution functions onto the moment space, with $\mathbf{f}$ and $\mathbf{f}^{\mathbf{eq}}$ being the density distribution functions and equilibrium distribution functions, respectively; $\mathbf{F_m}$ is the moment of the force term.

Without loss of generality, the two-dimensional nine-velocity (D2Q9) model is adopted in the present work, in which the discrete velocities c_i are given by

$$c_i = \begin{cases} c(0, 0), & i = 0 \\ c\left[\frac{\cos(i-1)\pi}{2}, \frac{\sin(i-1)\pi}{2}\right], & i = 1, 2, 3, 4, \\ \sqrt{2}c\left[\frac{\cos(2i-1)\pi}{4}, \frac{\sin(2i-1)\pi}{4}\right], & i = 5, 6, 7, 8 \end{cases}$$
(2)

where c represents the lattice speed ($c = \delta_x/\delta_t$; δ_x and δ_t are lattice spacing and time step, respectively) and is set as velocity unit. With the adopted D2Q9 model, the transformation matrix $\mathbf{M}$ is given by [38]

$$\mathbf{M} = \begin{pmatrix} -1 & -1 & -1 & -1 & -1 & -1 & -1 & -1 & -1 \\ -4 & -1 & -1 & -1 & -1 & -2 & -2 & -2 & -2 \\ -4 & -2 & -2 & -2 & -2 & -1 & -1 & -1 & -1 \\ -0 & -1 & -0 & -1 & -0 & -1 & -1 & -1 & -1 \\ -0 & -2 & -0 & -2 & -0 & -1 & -1 & -1 & -1 \\ -0 & -0 & -1 & -0 & -1 & -1 & -1 & -1 & -1 \\ -0 & -0 & -2 & -0 & -2 & -1 & -1 & -1 & -1 \\ -0 & -1 & -1 & -1 & -1 & -0 & -0 & -0 & -0 \\ -0 & -0 & -0 & -0 & -0 & -1 & -1 & -1 & -1 \end{pmatrix},$$
(3)

and the corresponding relaxation matrix $\mathbf{S}$ is defined as

$$\mathbf{S} = \mathrm{diag}(\tau_\rho, \tau_e, \tau_\epsilon, \tau_j, \tau_q, \tau_j, \tau_q, \tau_s, \tau_s)^{-1}.$$
(4)

The equilibrium density distribution function $\mathbf{f^{eq}}$ can be expressed as

$$f_i^{\text{eq}} = \omega_i \rho \left[1 + \frac{\mathbf{c_i} \cdot \mathbf{u}}{c_s^2} + \frac{(\mathbf{c_i} \cdot \mathbf{u})^2}{2c_s^2} - \frac{\mathbf{u}^2}{2c_s^2} \right], \quad (5)$$

where $c_s = c/\sqrt{3}$ is the lattice sound speed, ρ is the density, $\mathbf{u}$ is the velocity, ω_i are the model-dependent weight coefficients taken as $\omega_0 = 4/9$, $\omega_1 = \omega_2 = \omega_3 = \omega_4 = 1/9$, and $\omega_5 = \omega_6 = \omega_7 = \omega_8 = 1/36$ in the present work.

The moments of the forcing term $\mathbf{F_m}$ are given by [39]

$$\mathbf{F_m} = \left(\mathbf{I} - \frac{\mathbf{S}}{2} \right) \mathbf{M}\overline{\mathbf{F}}, \quad (6)$$

in which $\mathbf{I}$ is the identity matrix, and $\overline{\mathbf{F}} = (\overline{F_0}, \overline{F_1}, ..., \overline{F_8})^T$ is related to the body force $\mathbf{F}$:

$$\overline{F_i} = \omega_i \left[\frac{\mathbf{c_i} \cdot \mathbf{F}}{c_s^2} + \frac{\mathbf{u}\mathbf{F} : (\mathbf{c_i}\mathbf{c_i} - c_s^2 \mathbf{I})}{c_s^4} \right]. \quad (7)$$

The macroscopic density ρ and velocity $\mathbf{u}$ of gas flow can be determined by f_i:

$$\rho = \sum_{i=0}^{8} f_i, \quad (8)$$

$$\rho\mathbf{u} = \sum_{i=0}^{8} \mathbf{c_i} f_i. \quad (9)$$

The fluid pressure, kinetic and bulk viscosities are calculated by

$$p = c_s^2 \rho, \quad (10)$$

$$\nu = c_s^2 \left(\tau_s - \frac{1}{2} \right) \delta_t, \quad (11)$$

$$\xi = c_s^2 \left(\tau_e - \frac{1}{2} \right) \delta_t. \quad (12)$$

The relaxation time τ_s can be calculated by

$$\tau_s = \frac{1}{2} + \sqrt{\frac{6}{\pi}} \frac{\lambda}{\delta_x}. \quad (13)$$

To minimize the fictitious slip velocity, the relaxation time τ_q is chosen as [17]

$$\tau_q = \frac{8\tau_s - 1}{16\tau_s - 8}. \quad (14)$$

The mean-free path of gas λ is determined by density, pressure, and viscosity through the following relationship [40]:

$$\lambda = \frac{\rho\nu}{p} \sqrt{\frac{\pi RT}{2}}, \quad (15)$$

and the Knudsen number is obtained as

$$\text{Kn} = \frac{\lambda}{L}, \quad (16)$$

where L represents the characteristic size of the system investigated.

FIG. 1. Schematic of curved boundary scheme.

III. CURVED-BOUNDARY SCHEME FOR SECOND-ORDER SLIP CONDITION

As pointed out in the Introduction, an accurate boundary scheme is important for LB simulation of micro-gas flow. In the present study, a curved-boundary scheme with second-order velocity slip condition is proposed based on direct discretization method. As shown in Fig. 1, $\mathbf{x_f}$ is the fluid boundary node adjacent to solid node $\mathbf{x_s}$, and the physical boundary is located between $\mathbf{x_f}$ and $\mathbf{x_s}$. The parameter q is used to consider the influence of actual offset between lattice node and physical boundary, which is defined by

$$q = \frac{|\mathbf{x_f} - \mathbf{x_{int}}|}{|\mathbf{x_f} - \mathbf{x_s}|}, \quad (17)$$

where $\mathbf{x_{int}}$ represents the node on the gas-solid interface.

During the streaming process, the lattice nodes with density distribution function $f_i(\mathbf{x_f})$ will reach the wall and bounce back. As the parameter $q = 1/2$, $f_i(\mathbf{x_f})$ will become $f_{\bar{i}}(\mathbf{x_f})$ after a time step, where $f_{\bar{i}}$ represents the distribution function with velocity $\mathbf{c_{\bar{i}}} = -\mathbf{c_i}$. Generally, the parameter q is not equal to $1/2$, and $f_{\bar{i}}(\mathbf{x_f})$ needs to be reconstructed. Lallemand and Luo [35] proposed an effective scheme, i.e., the IBB method for this situation, in which the interpolation and bounce-back methods are combined. The value of $f_{\bar{i}}(\mathbf{x_f})$ can be reconstructed through a quadratic interpolation, which involves the values of three lattice nodes: $\mathbf{x_f}$, $\mathbf{x_{f'}} = \mathbf{x_f} + \mathbf{c_{\bar{i}}}\delta_t$, and $\mathbf{x_{f''}} = \mathbf{x_f} + 2\mathbf{c_{\bar{i}}}\delta_t$. The interpolation formulas of IBB method are as follows:

$$f_{\bar{i}}t(\mathbf{x_f}, t) = \begin{cases} q(1+2q)f_i^*(\mathbf{x_f}, t) + (1-4q^2)f_i^*(\mathbf{x_{f'}}, t) \\ -q(1-2q)f_i^*(\mathbf{x_{f''}}, t) + (\mathbf{c_i} \cdot \mathbf{u_g}), \quad q < \frac{1}{2} \\ \frac{1}{q(1+2q)}f_i^*(\mathbf{x_f}, t) + \frac{2q-1}{q}f_{\bar{i}}(\mathbf{x_{f'}}, t) \\ -\frac{2q-1}{2q+1}f_{\bar{i}}(\mathbf{x_{f''}}, t) + \frac{3z_i}{q(2q+1)}(\mathbf{c_i} \cdot \mathbf{u_g}), \quad q \geqslant \frac{1}{2} \end{cases} \quad (18)$$

TABLE I. Slip velocity models adopted in different slip boundary schemes.

Boundary schemes	Slip velocity models adopted
Halfway DBB [23]	$\mathbf{u_{slip}} = \frac{2-\sigma_v}{\sigma_v}\left(1.1464\lambda\frac{\partial \mathbf{u_g}}{\partial \mathbf{n}} - 0.9755\lambda^2\frac{\partial^2 \mathbf{u_g}}{\partial \mathbf{n}^2}\right)\big|_w$
Modified DBB [27]	$\mathbf{u_{slip}} = \frac{2-\sigma_v}{\sigma_v}\left(0.8183\lambda\frac{\partial \mathbf{u_g}}{\partial \mathbf{n}} - 0.6532\lambda^2\frac{\partial^2 \mathbf{u_g}}{\partial \mathbf{n}^2}\right)\big|_w$
NEE-CE [32]	$\mathbf{u_{slip}} = \frac{2-\sigma_v}{\sigma_v}\left(-\lambda\frac{\mathbf{u_g}}{r} + \lambda\frac{\partial \mathbf{u_g}}{\partial \mathbf{n}}\right)\big|_w$
Present scheme	$\mathbf{u_{slip}} = \frac{2-\sigma_v}{\sigma_v}\left(-\lambda\frac{\mathbf{u_g}}{r} + \lambda\frac{\partial \mathbf{u_g}}{\partial \mathbf{n}} + \frac{\lambda^2}{2!}\frac{\partial^2 \mathbf{u_g}}{\partial \mathbf{n}^2}\right)\big|_w$

in which

$$z_i = \begin{cases} \frac{2}{9} & i = 1-4 \\ \frac{2}{36} & i = 5-8 \end{cases}, \quad (19)$$

and the notation f_i^* represents the post-collision distribution function before the streaming process. $\mathbf{u_g}$ is the gas velocity at the gas-solid interface $\mathbf{x_{int}}$, which equals the velocity of moving boundary $\mathbf{u_w}$ in the continuum regime ($\mathrm{Kn} \leqslant 0.001$). However, in the slip regime ($0.001 < \mathrm{Kn} \leqslant 0.1$), the gas velocity $\mathbf{u_g}$ at the gas-solid interface $\mathbf{x_{int}}$ is not the same as the wall velocity $\mathbf{u_w}$, and the velocity slip $\mathbf{u_{slip}} = \mathbf{u_g} - \mathbf{u_w}$ occurs on the interface. At present, the appropriate second-order slip velocity model for curved boundaries is scarce in the literature; thus, we will deduce it in the following based on previous works [24,41].

Beskok *et al.* [41] have proposed a widely acknowledged second-order slip velocity model for straight boundaries, which is

$$\mathbf{u_{slip}} = \mathbf{u_g} - \mathbf{u_w} = \frac{2-\sigma_v}{\sigma_v}\left(\lambda\frac{\partial \mathbf{u_g}}{\partial \mathbf{n}} + \frac{\lambda^2}{2!}\frac{\partial^2 \mathbf{u_g}}{\partial \mathbf{n}^2}\right)\bigg|_w, \quad (20)$$

where $\partial/\partial \mathbf{n}$ denotes the gradient in the normal direction, σ_v is the tangential momentum accommodation coefficient (TMAC), and λ is the mean-free path of gas. Note that Eq. (20) was proposed for straight boundaries; it neglects the influence of boundary curvature, and cannot be used for curved boundaries [42]. Sun *et al.* [24] considered the influence of boundary curvature and derived a first-order slip velocity model for curved boundaries, which is

$$\mathbf{u_{slip}} = \frac{2-\sigma_v}{\sigma_v}\left(-\lambda\frac{\mathbf{u_g}}{r} + \lambda\frac{\partial \mathbf{u_g}}{\partial \mathbf{n}}\right)\bigg|_w, \quad (21)$$

where r is the curvature radius of boundary, and the term $-\lambda\frac{\mathbf{u_g}}{r}$ represents the influence of boundary curvature. Note that for a straight boundary with $r \to \infty$, the influence of boundary curvature can be ignored, and Eq. (21) reduces to the Maxwell first-order slip model for straight boundaries.

As analyzed above, Eq. (20) proposed by Beskok *et al.* [41] considers the influence of second-order slip ($\frac{\lambda^2}{2!}\frac{\partial^2 \mathbf{u_g}}{\partial \mathbf{n}^2}$) but ignores the influence of boundary curvature ($-\lambda\frac{\mathbf{u_g}}{r}$), while Eq. (21) proposed by Sun *et al.* [41] considers the influence of boundary curvature ($-\lambda\frac{\mathbf{u_g}}{r}$), but ignores the influence of second-order slip ($\frac{\lambda^2}{2!}\frac{\partial^2 \mathbf{u_g}}{\partial \mathbf{n}^2}$). To comprehensively incorporate the influences of second-order slip and boundary curvature, we deduce a second-order slip velocity model for curved boundaries based on the models of Beskok *et al.* [41] and Sun

et al. [24], which is

$$\mathbf{u_{slip}} = \frac{2-\sigma_v}{\sigma_v}\left(-\lambda\frac{\mathbf{u_g}}{r} + \lambda\frac{\partial \mathbf{u_g}}{\partial \mathbf{n}} + \frac{\lambda^2}{2!}\frac{\partial^2 \mathbf{u_g}}{\partial \mathbf{n}^2}\right)\bigg|_w. \quad (22)$$

Table I lists the present slip velocity model [Eq. (22)] and those adopted in previous slip boundary schemes [23,27,32]. It is shown that the slip velocity models adopted in the halfway DBB scheme [23] and modified DBB scheme [27] neglected the influence of boundary curvature; the slip velocity model adopted in the NEE-CE scheme [32] ignored the influence of second-order slip term, while the present slip velocity model considers both influences of second-order slip velocity and boundary curvature.

Upon the proposed slip velocity model [Eq. (22)], the counter-extrapolation method is utilized [33], in which the velocity gradients ($\partial \mathbf{u_g}/\partial \mathbf{n}$, $\partial^2 \mathbf{u_g}/\partial \mathbf{n}^2$) are directly discretized by velocity of nodes on the normal direction. For the normal vector n in Eq. (22), points $\mathbf{x'}$, $\mathbf{x''}$, $\mathbf{x'''}$, and $\mathbf{x''''}$ (see in Fig. 1) in fluid-phase region are selected for discretization, with $|\mathbf{x''''} - \mathbf{x'''}| = |\mathbf{x'''} - \mathbf{x''}| = |\mathbf{x''} - \mathbf{x'}| = |\mathbf{x'} - \mathbf{x_{int}}| = \delta$. It should be noted that the value of δ should be carefully chosen, as a small δ may cause the surrounding points being the solid points while a large δ may lead to larger truncation errors due to coarser discretization [43]. Following suggestions from previous literature [32,33,43,44], δ is set as $1.5\delta_x$ in the present work to make sure all the adjacent nodes (such as $\mathbf{x'_1}$, $\mathbf{x'_2}$, $\mathbf{x'_3}$, and $\mathbf{x'_4}$) are in fluid-phase region and maintain a good accuracy at the same time. The velocity $\mathbf{u'}$ at point $\mathbf{x'}$ is calculated based on the bilinear interpolation (BI) method [33]:

$$\mathbf{u'} \approx \frac{A_1\mathbf{u}(\mathbf{x'_3}) + A_2\mathbf{u}(\mathbf{x'_4}) + A_3\mathbf{u}(\mathbf{x'_1}) + A_4\mathbf{u}(\mathbf{x'_2})}{\delta^2}, \quad (23)$$

where A_1, A_2, A_3, and A_4 are areas of four subregions around point $\mathbf{x'}$. $\mathbf{u''}$, $\mathbf{u'''}$, and $\mathbf{u''''}$ at point x'', x''', and x'''' are obtained with the same process, respectively. With the obtained $\mathbf{u'}$, $\mathbf{u''}$, $\mathbf{u'''}$, and $\mathbf{u''''}$, the discretization form of velocity gradients can be obtained.

Note that the fictitious slip velocity may be induced by the IBB scheme [37], and deviation will be amplified if the fictitious slip velocity is involved in the discretization of the normal gradients. Thus, to exclude the influence of fictitious velocity, the explicit form of CE is utilized in the present work, where the normal gradients are discretized explicitly using a second-order forward finite-difference method:

$$\frac{\partial \mathbf{u_g}}{\partial \mathbf{n}} = \frac{-\frac{5}{2}\mathbf{u'} + 4\mathbf{u''} - \frac{3}{2}\mathbf{u'''}}{\delta}, \quad (24)$$

$$\frac{\partial^2 \mathbf{u_g}}{\partial \mathbf{n}^2} = \frac{3\mathbf{u'} - 8\mathbf{u''} + 7\mathbf{u'''} - 2\mathbf{u''''}}{\delta^2}. \quad (25)$$

As the constant coefficients of velocity on the normal points sum up to zero in both Eq. (24) and Eq. (25), the fictitious slip term is eliminated from the explicit discretization (assuming that the fictitious slip velocities on the normal points are the same), ensuring the accuracy of the predicted slip velocity. Using the same explicit CE method, the term $-\lambda \frac{\mathbf{u_g}}{r}$ can be discretized as

$$-\lambda \frac{\mathbf{u_g}}{r} = -\lambda \frac{3\mathbf{u}' - 3\mathbf{u}'' + \mathbf{u}'''}{r}. \quad (26)$$

It should be pointed out that Eq. (26) would induce the fictitious slip term. However, since the curvature radius r is normally much larger than lattice space δ_x, the influence of this error term is minor.

Substituting Eqs. (24)–(26) into Eq. (22), the slip velocity $\mathbf{u_{slip}}$ can be obtained as

$$\mathbf{u_{slip}} = \frac{2 - \sigma_v}{\sigma_v} \left(\lambda \frac{-\frac{5}{2}\mathbf{u}' + 4\mathbf{u}'' + \frac{3}{2}\mathbf{u}'''}{\delta} \right.$$
$$\left. + \frac{\lambda^2}{2} \frac{3\mathbf{u}' - 8\mathbf{u}'' + 7\mathbf{u}''' - 2\mathbf{u}''''}{\delta^2} - \lambda \frac{3\mathbf{u}' - 3\mathbf{u}'' + \mathbf{u}'''}{r} \right). \quad (27)$$

As a comparison, the discretized second-order slip velocity formula obtained with the same implicit CE method as applied by Liu *et al.* [32] is given here:

$$\mathbf{u_{slip}} = \frac{1}{\frac{\sigma_v}{2-\sigma_v} + \frac{\lambda}{r} + 3\lambda - \frac{4}{9}\lambda^2} \left(\lambda \frac{6\mathbf{u}' - \frac{3}{2}\mathbf{u}'' - \frac{9}{2}\mathbf{u_w}}{\delta} \right.$$
$$\left. - \frac{\lambda^2}{2} \frac{-5\mathbf{u}' + 4\mathbf{u}'' - \mathbf{u}''' + 2\mathbf{u_w}}{\delta^2} - \lambda \frac{\mathbf{u_w}}{r} \right). \quad (28)$$

It can be seen that the implicit CE method induces the fictitious slip velocity because the sum of constant coefficients of velocities on the normal nodes in Eq. (28) is not equal to zero.

For the convenience of future usage, the implementation process of the slip boundary scheme proposed in this study can be briefly summarized as the following steps:

(1) Determine the boundary nodes ($\mathbf{x_f}$) and the corresponding adjacent lattice nodes ($\mathbf{x_{f'}}$, $\mathbf{x_{f''}}$) for the calculation of unknown density distribution functions.

(2) Calculate parameter q for all boundary nodes through Eq. (17).

(3) Determine the points on the normal direction ($\mathbf{x}'$, $\mathbf{x}''$, $\mathbf{x}'''$, and $\mathbf{x}''''$) and the corresponding surrounding points for intersection (such as $\mathbf{x}'_1$, $\mathbf{x}'_2$, $\mathbf{x}'_3$, and $\mathbf{x}'_4$).

(4) Calculate the corresponding velocity of normal points by Eq. (23) derived from the BI method.

(5) Calculate the slip velocity $\mathbf{u_{slip}}$ by Eq. (27) derived from the explicit CE method.

(6) Substitute the gas velocity $\mathbf{u_g}$ in Eq. (18) with $\mathbf{u_g} = \mathbf{u_{slip}} + \mathbf{u_w}$.

(7) Stream for the next time step.

Note that the first three steps only need to be done once for a stationary boundary, while the later steps need to be done in every iteration steps.

IV. NUMERICAL TESTS AND DISCUSSION

To prove the accuracy of the proposed boundary scheme in this study, the microscale gas flows are numerically simulated using the MRT-LB model with the IBB-ECE boundary scheme proposed in Sec. III. The numerical benchmarks include force-driven gas flow in horizontal (inclined) microchannel, gas flow around a micro-cylinder, and Couette flow between two micro-cylindrical surfaces. The numerical predictions with the present IBB-ECE scheme are compared with the analytical solutions obtained with proposed slip velocity model and the predictions by other schemes in the literature.

A. Force-driven gas flow in horizontal microchannel

The force-driven gas flow in a horizontal microchannel is presented in Fig. 2. The driven force is $G_x = \frac{\partial p}{\partial x} = 10^{-4}$. The actual offsets between the upper (lower) wall and the boundary lattice nodes varies ($q\delta_x$, $q = 0.25, 0.5, 0.75, 1.0$) to test the accuracy of the present IBB-ECE scheme, and the inlet and outlet boundary conditions of the microchannel are set as periodic ones.

For the force-driven gas flow in a microchannel as shown in Fig. 2, the velocity profile along the y direction with second-order slip condition in the microchannel can be obtained analytically by [45]

$$u(y) = \frac{G_x H^2}{2\mu} \left[\frac{y}{H} - \left(\frac{y}{H} \right)^2 + \frac{2 - \sigma_v}{\sigma_v} (\mathrm{Kn} - \mathrm{Kn}^2) \right], \quad (29)$$

where H is the height of the microchannel, $\mathrm{Kn} = \lambda/H$, and σ_v is the tangential accommodation coefficient, which is chosen as 1 for a fully diffusive wall.

In order to quantitatively compare the precisions of different slip boundary schemes, the maximum relative deviation and the relative standard deviation (RSD) are analyzed in this work, which are defined as follows:

$$E_{\max} = \max \left\{ \left| \frac{\mathbf{u}_{\mathrm{numer}}(i, j) - \mathbf{u}_{\mathrm{anal}}(i, j)}{\mathbf{u}_{\mathrm{anal}}(i, j)} \right| \right\}, \quad (30)$$

$$E_{\mathrm{RSD}} = \sqrt{\frac{\sum_{ij} [\mathbf{u}_{\mathrm{numer}}(i, j) - \mathbf{u}_{\mathrm{anal}}(i, j)]^2}{\sum_{ij} [\mathbf{u}_{\mathrm{anal}}(i, j)]^2}}, \quad (31)$$

where $\mathbf{u}_{\mathrm{numer}}(i, j)$ and $\mathbf{u}_{\mathrm{anal}}(i, j)$ are the velocities at location (i, j) obtained with numerical and analytical approaches, respectively.
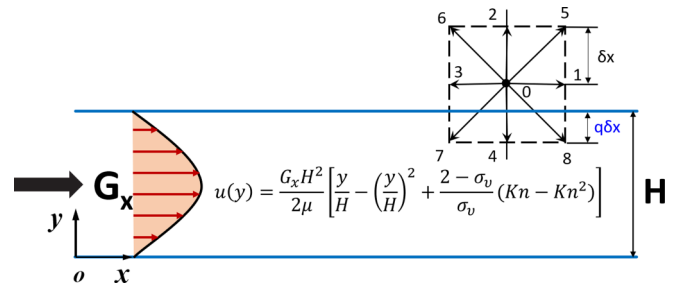

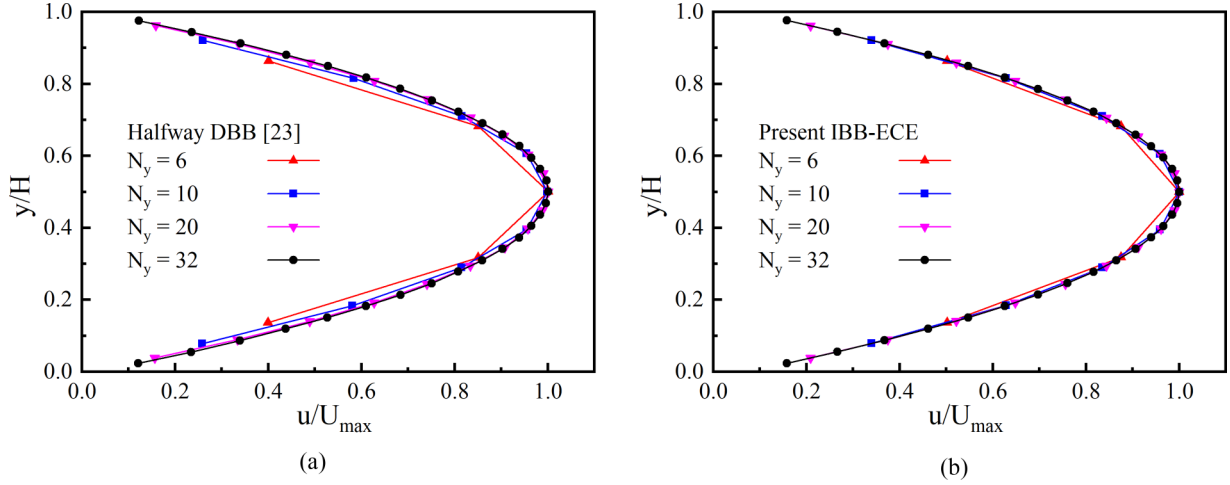FIG. 2. Force-driven gas flow in horizontal microchannel

FIG. 3. Velocity profiles along y direction in horizontal microchannel under different values of N_y(Kn = 0.0194, $q = 0.25$) predicted by halfway DBB scheme [23] (a) and present IBB-ECE scheme (b).

The grid refinement studies are performed in this work. Figure 3 compares the results by the present IBB-ECE scheme and the halfway DBB scheme [23] when Kn = 0.0194 and $q = 0.25$. While the results predicted by the halfway DBB scheme deteriorate rapidly with reduced lattice number (N_y decreasing from $32\delta_x$ to $6\delta_x$), the results obtained by the present IBB-ECE scheme are quite robust. It can be observed that the results remain accurate even under the least lattice number ($N_y = 6\delta_x$), showing a good robustness of the present scheme. Considering computational accuracy and efficiency, the uniform lattice nodes $N_x \times N_y = 10 \times 32$ are adopted for this case.

Table II shows the effects of eliminating the fictitious slip velocity through the comparison between results obtained by the present explicit counter-extrapolation (ECE) method [see Eq. (27)] and the implicit CE method [see Eq. (28)]. It can be seen that although the results obtained by the implicit method remain accurate under $q = 0.5$ with the help of choosing the appropriate relaxation time, the accuracy deteriorates violently when $q \neq 0.5$, since the fictitious slip velocity is involved in the implicit discretization and amplified during iterations. However, the present explicit scheme significantly improves the accuracy when q varies from 0 to 1.0, making it a more promising treatment for predicting the slip velocity.

Figure 4 shows the normalized velocity profiles in the microchannel under different values of Kn and q. The predicted velocity distributions obtained by the halfway DBB scheme [23], NEE-CE scheme [32], and present IBB-ECE scheme

are compared with the analytical solutions, respectively. It shows that the results based on the halfway DBB scheme are not precise enough, especially for the lattice nodes closer to the boundary. Moreover, the accuracy of the halfway DBB scheme deteriorates as the virtual boundary deviates from physical boundary (i.e., as q increases). The accuracy of the NEE-CE scheme is better than that of the halfway DBB scheme, but deviations still exist when compared with the analytical solutions It shows that for the present IBB-ECE scheme, the predicted results coincide well with the analytical solutions, and the value of q has minor influence on the numerical accuracy.

To show it more clearly, the maximum relative deviations and relative standard deviations of the predictions using the above three schemes under different values of Kn and q are presented in Table III. It shows that the present IBB-ECE scheme provides the most accurate predictions under different parameter arrangements, while it is hard for both halfway DBB scheme and NEE-CE scheme to capture the velocity slip accurately under the conditions with larger Kn numbers. The reasons for the deviation are two-fold. Firstly, the slip velocity models achieved by both halfway DBB and NEE-CE cannot illustrate the slip boundary condition accurately (as illustrated in Sec. III), which leads to deviation from the present results. In addition, the halfway DBB scheme can only restore the slip boundary condition with $q = 0.5$, while the NEE-CE scheme also suffers from the influence of fictitious slip velocity when $q \neq 0.5$, both leading to deviations significantly larger than the present results.

TABLE II. Comparisons of maximum relative deviations and relative standard deviations caused by explicit and implicit CE methods under different values of q (Kn = 0.0194).

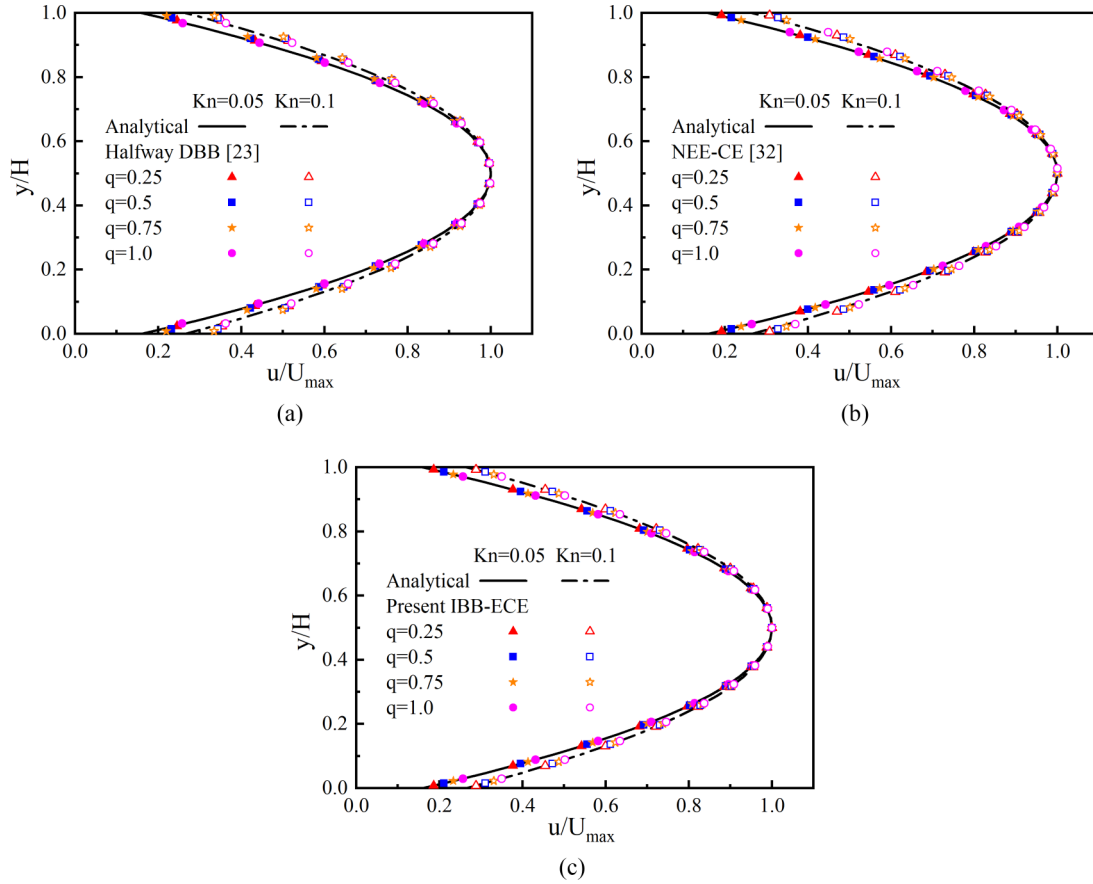| Deviations	CE methods	$q = 0.25$	$q = 0.5$	$q = 0.75$	$q = 1.0$
E_{max}	Explicit scheme	2.68×10^{-3}	1.71×10^{-3}	2.43×10^{-3}	3.22×10^{-3}
[Eq. (30)]	Implicit scheme	7.99×10^{-3}	1.70×10^{-3}	7.14×10^{-3}	1.01×10^{-2}
E_{RSD}	Explicit scheme	5.36×10^{-4}	3.42×10^{-4}	5.09×10^{-4}	6.05×10^{-4}
[Eq. (31)]	Implicit scheme	1.61×10^{-3}	3.39×10^{-4}	1.43×10^{-3}	2.52×10^{-3}

FIG. 4. Comparisons of velocity profiles along y direction in horizontal microchannel under different values of Kn and q predicted by halfway DBB scheme [23] (a), NEE-CE scheme [32] (b), and present IBB-ECE scheme (c) with analytical solutions given by Eq. (29).

B. Force-driven flow in inclined microchannel

The force-driven gas flow in an inclined microchannel as shown in Fig. 5 is also simulated to validate the superiority of the present second-order slip boundary scheme (IBB-ECE). Three different inclination angles θ ($\tan\theta = 0.46$, 1.2, and 3.72) are employed in the simulation. Uniform lattices are adopted in the present model ($N_x \times N_y = 100 \times 100$ and $N_{y'} = N_y + N_x \tan\theta$). The inlet and outlet boundary conditions of the microchannel are set as periodic ones.

Figure 6 shows the velocity distributions in the y' direction for different θ predicted by different boundary schemes, in which the numerical predictions based on the proposed IBB-ECE scheme agree well with the analytical velocity profile. However, the velocities predicted by the halfway DBB scheme [23] are smaller than the analytical results, while the NEE-CE scheme [32] overestimates the gas velocities. The maximum relative deviations and relative standard deviations of the present IBB-ECE scheme are compared with those of

TABLE III. Maximum relative deviations and relative standard deviations of velocities predicted by halfway DBB [23], NEE-CE [32], and present IBB-ECE schemes under different values of Kn and q.

Deviations	Schemes	Kn	$q = 0.25$	$q = 0.5$	$q = 0.75$	$q = 1.0$
	Halfway DBB [23]	0.05	9.23×10^{-2}	8.14×10^{-2}	7.67×10^{-2}	5.68×10^{-2}
$E_{\max}$		0.1	1.10×10^{-1}	9.82×10^{-2}	7.85×10^{-2}	6.14×10^{-2}
	NEE-CE	0.05	3.72×10^{-2}	3.14×10^{-2}	2.57×10^{-2}	2.74×10^{-2}
[Eq. (30)]	[32]	0.1	7.15×10^{-2}	6.40×10^{-2}	5.86×10^{-2}	5.43×10^{-2}
	Present IBB-ECE	0.05	4.67×10^{-3}	2.43×10^{-3}	3.68×10^{-3}	6.71×10^{-3}
		0.1	6.36×10^{-3}	3.73×10^{-3}	5.42×10^{-3}	8.47×10^{-3}
	Halfway DBB [23]	0.05	4.67×10^{-2}	1.34×10^{-2}	2.79×10^{-2}	3.11×10^{-2}
E_{RSD}		0.1	4.99×10^{-2}	1.56×10^{-2}	2.48×10^{-2}	3.00×10^{-2}
	NEE-CE	0.05	4.54×10^{-3}	4.10×10^{-3}	3.37×10^{-3}	3.59×10^{-3}
[Eq. (31)]	[32]	0.1	1.27×10^{-2}	1.19×10^{-2}	1.12×10^{-2}	1.04×10^{-2}
	Present IBB-ECE	0.05	6.08×10^{-4}	3.49×10^{-4}	5.12×10^{-4}	8.07×10^{-4}
		0.1	8.91×10^{-4}	5.01×10^{-4}	6.98×10^{-4}	9.98×10^{-4}

TABLE IV. Maximum relative deviations and relative standard deviations of velocities predicted by halfway DBB [23], NEE-CE [32], and present IBB-ECE schemes under different values of Kn and θ.

Deviations	Schemes	Kn	$\tan\theta = 0.46$	$\tan\theta = 1.2$	$\tan\theta = 3.72$
	Halfway DBB [23]	0.05	6.46×10^{-2}	8.72×10^{-2}	7.12×10^{-2}
$E_{\max}$		0.1	2.11×10^{-1}	2.97×10^{-1}	2.38×10^{-1}
[Eq. (30)]	NEE-CE [32]	0.05	3.85×10^{-2}	3.90×10^{-2}	3.89×10^{-2}
		0.1	7.24×10^{-2}	7.29×10^{-2}	7.38×10^{-2}
	Present IBB-ECE	0.05	3.27×10^{-3}	1.54×10^{-3}	6.01×10^{-3}
		0.1	6.67×10^{-3}	2.68×10^{-3}	1.02×10^{-2}
	Halfway DBB [23]	0.05	6.18×10^{-3}	1.78×10^{-2}	1.02×10^{-2}
E_{RSD}		0.1	2.79×10^{-2}	4.01×10^{-2}	3.88×10^{-2}
[Eq. (31)]	NEE-CE [32]	0.05	4.10×10^{-3}	4.34×10^{-3}	5.46×10^{-3}
		0.1	1.21×10^{-2}	1.22×10^{-2}	1.43×10^{-2}
	Present IBB-ECE	0.05	5.13×10^{-4}	2.02×10^{-4}	7.34×10^{-4}
		0.1	7.99×10^{-4}	4.01×10^{-4}	2.88×10^{-3}

the halfway DBB scheme and NEE-CE scheme in Table IV. We can see that the halfway DBB scheme deviates most among the three schemes due to the fact that it can only restore the slip velocity model with $q = 0.5$. Deviations for the NEE-CE scheme are also non-neglectable, especially for Kn = 0.1, where the second-order velocity slip term becomes large and the influence of fictitious slip velocity also exists. It is obvious that both the maximum relative deviations and relative standard deviations of the proposed IBB-ECE scheme are significantly smaller than those of the halfway DBB scheme and NEE-CE scheme at different values of Kn and θ.

C. Gas flow around a micro-cylinder

In this section, the gas flow around a micro-cylinder as shown in Fig. 7 is simulated to show the effect of the second-order slip term $\frac{\lambda^2}{2!}\frac{\partial^2 \mathbf{u_g}}{\partial \mathbf{n}^2}$ adopted in the present boundary scheme on the gas velocity at the gas-solid interface. The Reynolds

FIG. 5. Force-driven gas flow in an inclined microchannel.

number of gas flow around a micro-cylinder is defined as

$$\mathrm{Re} = \frac{U_\infty D}{\nu}, \qquad (32)$$

where U_∞ is the incoming gas velocity and D is the diameter of the micro-cylinder. As shown in Fig. 7, the uniform lattices are adopted in a computational region of $40D \times 20D$ in the simulation after a grid independence test ($\delta_x = \frac{1}{30}D$). The boundary conditions are set as follows: at inlet: $u_x = U_\infty$, $u_y = 0$; at outlet: $\frac{\partial u_x}{\partial x} = \frac{\partial u_y}{\partial x} = 0$; at top and bottom boundaries: $\frac{\partial u_x}{\partial y} = \frac{\partial u_y}{\partial y} = 0$. The streamlines around the cylinder are also presented in Fig. 7, in which the velocity slip effect is obviously seen in microgas flow (Kn = 0.015) when compared with the macroscale flow (Kn = 0.0) at the same Reynolds number. As the slip phenomenon exists on the solid-gas interface, the kinetic energy of gas flow in the boundary layer increases; therefore, the separation phenomenon occurs backward and the corresponding trailing vortex region shrinks.

Figure 8 compares the normalized slip velocity distributions along the micro-cylinder surface, which are obtained by the present IBB-ECE scheme (adopting the second-order slip velocity model), the modified DBB scheme (adopting the second-order slip velocity model) [27], the NEE-CE method (adopting the first-order slip velocity model) [32], and the finite-difference method (FDM) (adopting the first-order slip velocity model) [46]. As shown in Fig. 8, the application of the second-order slip term $\frac{\lambda^2}{2!}\frac{\partial^2 \mathbf{u_g}}{\partial \mathbf{n}^2}$ causes significant differences in the prediction of slip velocity, especially under the condition with relatively larger Knudsen number. The predicted slip velocities by adopting the second-order slip model are significantly smaller as compared with those obtained by adopting the first-order slip model. Also, note that there exists a little difference between the results obtained by the present IBB-ECE scheme and those obtained by modified DBB scheme, which is due to the ignorance of the influence of boundary curvature in the latter scheme (see Table I). However, this difference is minor when compared with the difference induced by neglecting the second-order slip term. Thus, it can be inferred that the second-order slip effect must be taken considered for an accurate simulation of microgas flow over
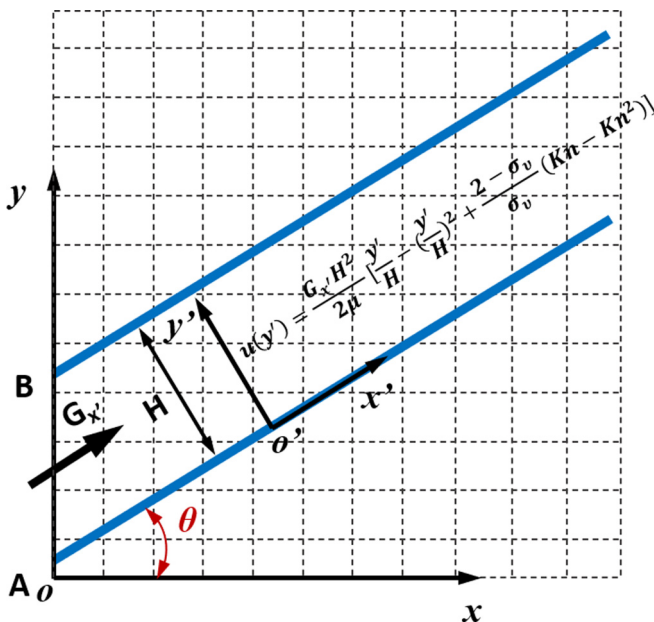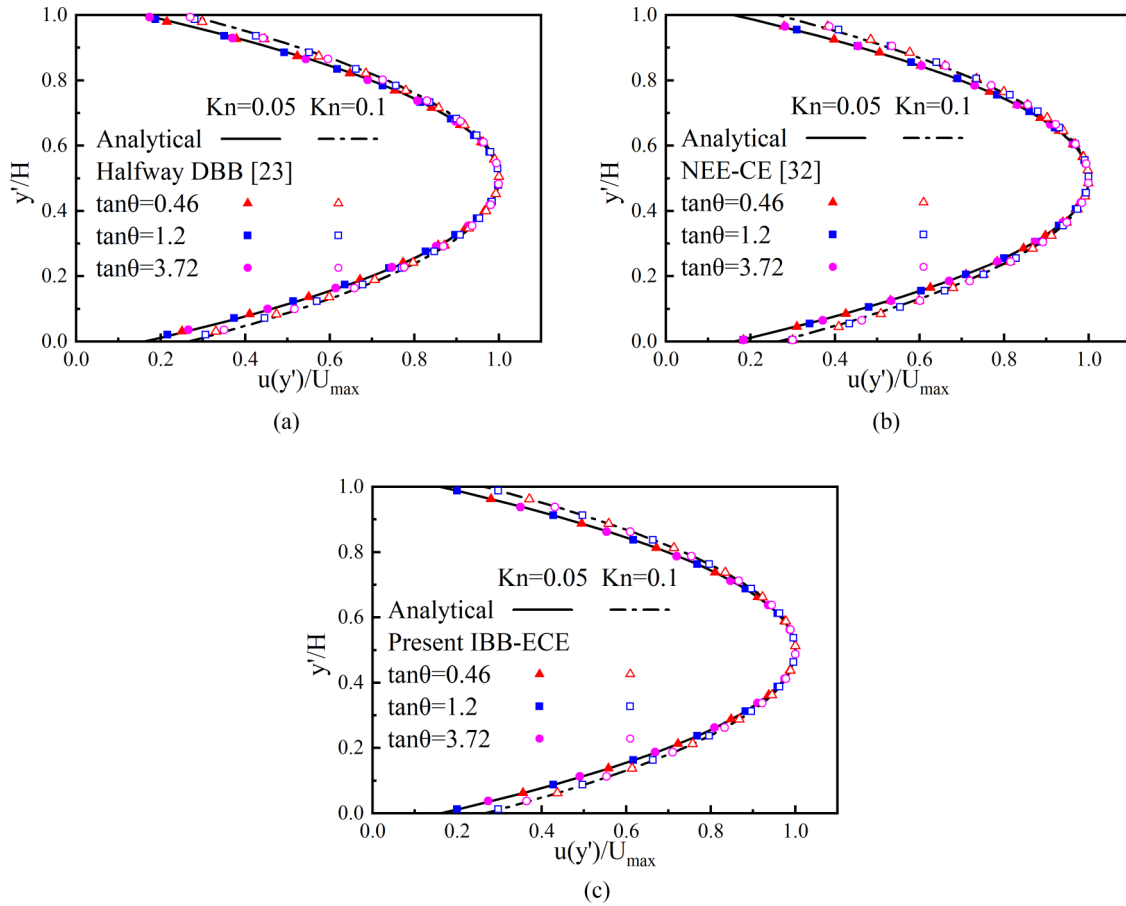
FIG. 6. Comparisons of velocity profiles along y' direction in inclined microchannel under different values of Kn and q predicted by halfway DBB scheme [23] (a), NEE-CE scheme [32] (b), and present IBB-ECE scheme (c) with the analytical solutions given by Eq. (29).

curved boundary, especially at a relatively larger Knudsen number.

D. Couette flow between two micro-cylindrical surfaces

In this section, the gas Couette flow between two cylindrical surfaces is numerically simulated to test the superiority of the proposed IBB-ECE scheme for a moving curved boundary. As shown in Fig. 9, the inner cylindrical surface with radius R_1 rotates at a fixed angular velocity ω while the outer cylindrical surface with radius R_2 keeps stationary. In a two-dimensional polar coordinate system (r, θ), the Navier-Stokes equations for the Couette flow shown in Fig. 9 can be

expressed as

$$\frac{d^2 u_\theta}{dr^2} + \frac{d}{dr}\left(\frac{u_\theta}{r}\right) = 0, \tag{33}$$

where u_θ is the tangential velocity of gas and r is the local curvature radius. With the proposed second-order slip boundary
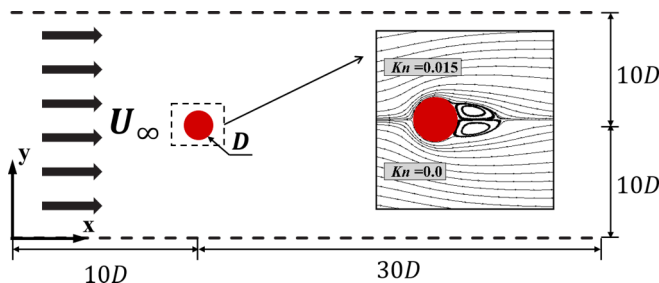
FIG. 7. Gas flow around a micro-cylinder.
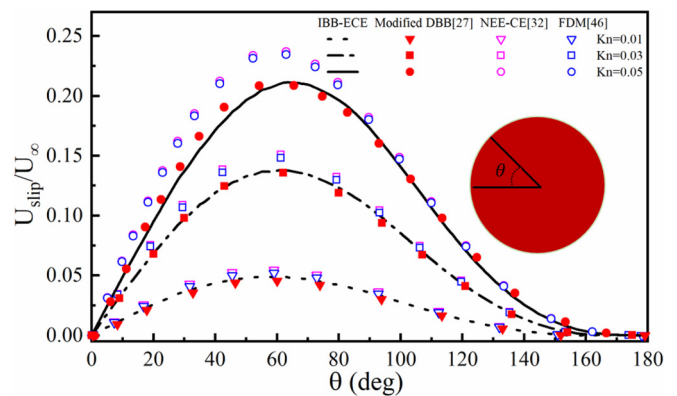
FIG. 8. Normalized slip velocity distributions along cylinder surface under different values of Kn predicted by different boundary schemes.
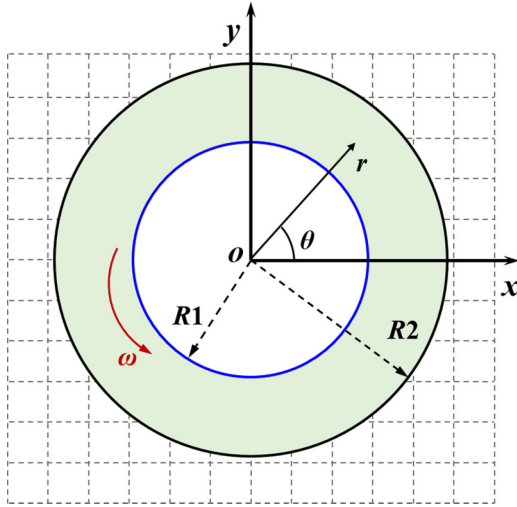
FIG. 9. Couette flow between two micro-cylindrical surfaces

model [i.e., Eq. (22)], the gas velocities on the inner and outer cylinder surfaces can be obtained as

$$u_\theta\big|_{r=R_1} = \omega R_1 + \frac{2-\sigma_{v1}}{\sigma_{v1}}\left(\lambda\frac{du_\theta}{dr} + \frac{\lambda^2}{2}\frac{d^2u_\theta}{dr^2} - \lambda\frac{u_\theta}{r}\right)\Bigg|_{r=R_1},$$

(34a)

$$u_\theta\big|_{r=R_2} = -\frac{2-\sigma_{v2}}{\sigma_{v2}}\left(\lambda\frac{du_\theta}{dr} + \frac{\lambda^2}{2}\frac{d^2u_\theta}{dr^2} - \lambda\frac{u_\theta}{r}\right)\Bigg|_{r=R_2},$$

(34b)

where σ_{v1}, σ_{v2} are the TMAC for the inner and outer surfaces, respectively, which are chosen as 1 for fully diffusive walls and can be removed from the above equations. Thus, the analytical tangential velocity profile under the second-order slip boundary condition can be obtained:

$$u_\theta = \frac{C_1}{r} + C_2 r,$$

(35)

where the parameters C_1 and C_2 are determined by

$$C_1 = \frac{R_1{}^4 R_2{}^4 \omega}{-R_1{}^4 R_2{}^2 + 2R_1{}^4 R_2\lambda - 2R_1{}^4\lambda^2 + R_1{}^2 R_2{}^4 + 2R_1 R_2{}^4\lambda - 2R_2{}^4\lambda^2},$$

(36a)

$$C_2 = \frac{-R_1{}^4 \omega(R_2{}^2 - 2R_2\lambda + 2\lambda^2)}{-R_1{}^4 R_2{}^2 + 2R_1{}^4 R_2\lambda - 2R_1{}^4\lambda^2 + R_1{}^2 R_2{}^4 + 2R_1 R_2{}^4\lambda - 2R_2{}^4\lambda^2},$$

(36b)

in which $\lambda = \text{Kn}(R_2 - R_1)$ is the mean-free path of gas, and R_1 and R_2 are chosen as $30\delta_x$ and $50\delta_x$, respectively.

The comparisons of normalized velocity $\frac{u_\theta}{\omega R_1}$, which were numerically obtained by different boundary schemes under $\text{Kn} = 0.05$ and $\text{Kn} = 0.1$, are demonstrated in Fig. 10. The numerical results predicted by the present IBB-ECE scheme agree well with the analytical solutions, except with a minor underestimation of gas velocity along the outer boundary. The predictions based on the halfway DBB scheme [23] do not agree well with the analytical results due to its truncation errors from the zigzag approximation and ignorance of the influence of boundary curvature (see Table I). The predictions

of the modified DBB scheme [27] also deviate from the analytical solutions near the boundary due to its ignorance of the influence of boundary curvature. Note that the NEE-CE scheme [32] deviates most from the analytical solutions because the second-order slip term is neglected (see Table I) and the fictitious slip velocity is not eliminated due to the implicit CE method adopted in this scheme. As the Knudsen number increases, the deviations of the halfway DBB, modified DBB, and NEE-CE schemes become larger, indicating that the present IBB-ECE scheme is a better slip boundary scheme for the moving curved boundary under relatively higher Knudsen numbers.
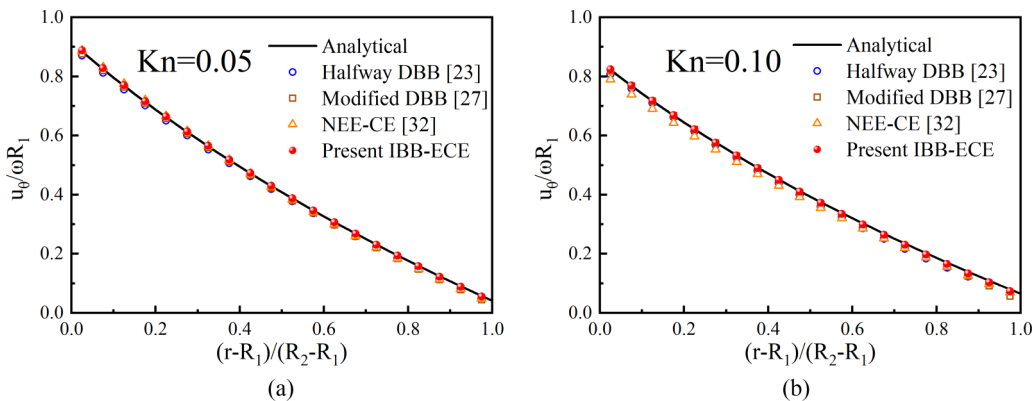

(a)

(b)

FIG. 10. Comparisons of normalized velocity profiles of Couette flow between two micro-cylindrical surfaces predicted by different slip boundary schemes with Kn = 0.05 (a) and Kn = 0.1 (b) with the analytical solutions given by Eq. (35).

TABLE V. Maximum relative deviations and relative standard deviations of velocities obtained by halfway DBB [23], modified DBB [27], NEE-CE [32], and present IBB-ECE schemes under different values of Kn.

Schemes	E_{max} [Eq. (30)]		E_{RSD} [Eq. (31)]	
	Kn = 0.05	Kn = 0.1	Kn = 0.05	Kn = 0.1
Halfway DBB [23]	9.87×10^{-2}	1.04×10^{-1}	2.98×10^{-2}	3.52×10^{-2}
Modified DBB [27]	1.76×10^{-1}	1.98×10^{-1}	2.13×10^{-2}	2.68×10^{-2}
NEE-CE [32]	1.60×10^{-1}	1.19×10^{-1}	3.85×10^{-2}	5.75×10^{-2}
Present IBB-ECE	4.12×10^{-2}	7.82×10^{-2}	6.71×10^{-3}	1.14×10^{-2}

The comparisons of maximum relative deviations and relative standard deviations caused by different schemes are presented in Table V. It can be seen that the present IBB-ECE scheme achieves the highest accuracy, while the three other schemes (halfway DBB scheme, modified DBB scheme, and NEE-CE scheme) fail to predict the velocity precisely, especially on the boundary nodes, where the slip velocity becomes the major concern.

The stability test of the present IBB-ECE scheme is also performed and presented in Fig. 11 to validate the consistency of the present scheme under a moving curved boundary. The predicted maximum normalized velocities $U_{max} = \frac{u_{\theta,max}}{\omega R_1}$ are compared with the analytical solutions under various Kn numbers within the slip regime ($0.001 \leqslant Kn \leqslant 0.1$). The results show that the present scheme reaches a good agreement with the analytical solutions under different Kn numbers. Thus, the present IBB-ECE scheme maintains a good stability against the variation of Kn numbers to achieve the second-order slip velocity condition. Furthermore, the experimental order of convergence for the IBB-ECE scheme is tested. All the discretization methods adopted in the IBB-ECE scheme is of second-order accuracy against δ_x in order to maintain the second-order accuracy of LB method. As shown in Fig. 12, the slopes of results obtained by the IBB-ECE coincide well with slope 2 under various Kn numbers, proving a second-order convergency.

V. CONCLUSIONS

In this paper, we have proposed an improved curved-boundary scheme with the second-order slip velocity condition (i.e., IBB-ECE scheme) for MRT-LB simulation of microgas flow in the slip regime (($0.001 < Kn \leqslant 0.1$)). The proposed IBB-ECE scheme is a combination of the interpolation bounce-back method for the density distribution functions on a curved boundary and the explicit counter-extrapolation method for gas slip velocity on gas-solid interface. The IBB method can well consider the effect of the offset between the lattice node and the physical boundary, while the developed ECE method can eliminate the influence of fictitious slip velocity on gas-solid interface by introducing the explicit extrapolation approach. To get a precise slip velocity on a curved wall, a slip velocity model, which incorporates both the effect of second-order velocity slip term and the effect of boundary curvature radius, is also developed in this work, from which the gas slip velocity on a curved wall is captured by discretizing the corresponding slip terms directly. The proposed second-order slip boundary scheme is then applied with the MRT-LB model and tested by simulating benchmark cases including the force-driven gas flow in horizontal (inclined) microchannel, the gas flow around a micro-cylinder, and the Couette flow between two micro-cylindrical surfaces. Numerical tests show that as compared with the halfway DBB, modified DBB, NEE-CE, and FDM schemes reported in the literature, the proposed IBB-ECE scheme is of the highest accuracy. Indeed, it should be admitted that the proposed IBB-ECE scheme scarifies a good locality by adopting more nodes on the normal direction, and may not be appropriate for coarser grids, but it achieves an improved numerical accuracy
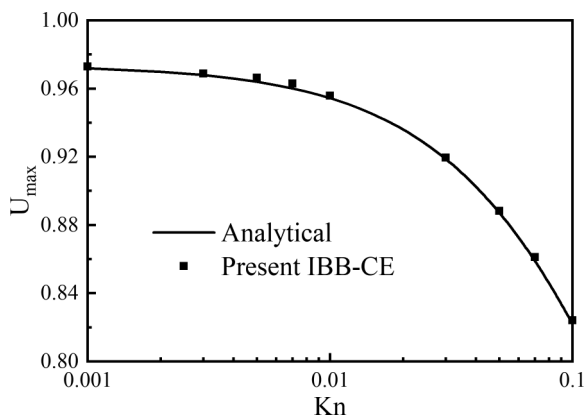

FIG. 11. Comparisons of maximum normalized velocities under various Kn numbers predicted by the present IBB-ECE scheme with analytical solutions given by Eq. (35).
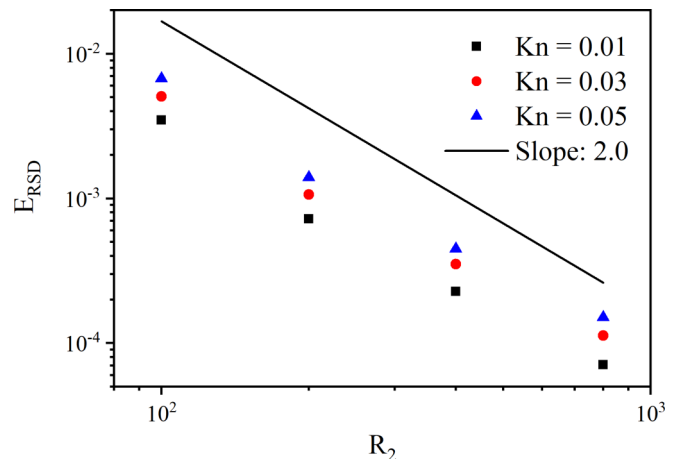

FIG. 12. Relative standard deviations under different lattice numbers and Kn; slope 2 indicates a second-order convergence.

and maintains robust results under reduced resolutions or increased Kn. It turns out that the IBB-ECE scheme proposed in this paper is a precise and easy implementing scheme for curved boundary with the second-order velocity slip condition.

[1] S. S. Hsieh and W. C. Chang, Microspray quenching on nanotextured surfaces via a piezoelectric atomizer with multiple arrays of micronozzles, Int. J. Heat Mass Transfer **121**, 832 (2018).

[2] M. Ansari and E. Amani, Micro-combustor performance enhancement using a novel combined baffle-bluff configuration, Chem. Eng. Sci. **175**, 243 (2018).

[3] Y. Zheng, T. D. Manh, N. D. Nam, M. Barzegar Gerdroodbary, R. Moradi, and I. Tlili, Optimization of micro Knudsen gas sensor for high precision detection of SO_2 in natural gas, Results Phys. **16**, 102933 (2020).

[4] Z. Liu, J. Zhou, and H. Wu, Non-isothermal slip flow over micro spherical particle at low Reynolds numbers, Chem. Eng. Sci. **191**, 19 (2018).

[5] Y. L. He, Q. Liu, Q. Li, and W. Q. Tao, Lattice Boltzmann methods for single-phase and solid-liquid phase-change heat transfer in porous media: A review, Int. J. Heat Mass Transfer **129**, 160 (2019).

[6] A. A. Avramenko, Y. Y. Kovetska, I. V. Shevchuk, A. I. Tyrinov, and V. I. Shevchuk, Heat transfer in porous microchannels with second-order slipping boundary conditions, Transp. Porous Media **129**, 673 (2019).

[7] L. de Luca Xavier Augusto, P. Tronville, J. A. S. Gonçalves, and G. C. Lopes, A simple numerical method to simulate the flow through filter media: Investigation of different fibre allocation algorithms, Can. J. Chem. Eng. **99**, 2760 (2021).

[8] Z. Guo, J. Qin, and C. Zheng, Generalized second-order slip boundary condition for nonequilibrium gas flows, Phys. Rev. E **89**, 013021 (2014).

[9] S. Tao, H. Zhang, and Z. Guo, Drag correlation for micro spherical particles at finite Reynolds and Knudsen numbers by lattice Boltzmann simulations, J. Aerosol Sci. **103**, 105 (2017).

[10] Z. Liu, Z. Mu, and H. Wu, Numerical modeling of slip flow and heat transfer over microcylinders with lattice Boltzmann method, J. Heat Transfer **141**, 042401 (2019).

[11] J. Horbach and S. Succi, Lattice Boltzmann versus Molecular Dynamics Simulation of Nanoscale Hydrodynamic Flows, Phys. Rev. Lett. **96**, 224503 (2006).

[12] S. Zhang, J. Tang, H. Wu, and R. Huang, Improved thermal multiple-relaxation-time lattice Boltzmann model for liquid-vapor phase change, Phys. Rev. E **103**, 043308 (2021).

[13] J. Tang, S. Zhang, and H. Wu, Multiphase flow simulation with three-dimensional weighted-orthogonal multiple-relaxation-time pseudopotential lattice Boltzmann model, Phys. Fluids **33**, 123305 (2021).

[14] X. Nie, G. D. Doolen, and S. Chen, Lattice-Boltzmann simulations of fluid flows in MEMS, J. Stat. Phys **107**, 279 (2002).

[15] S. Ansumali and I. V. Karlin, Kinetic boundary conditions in the lattice Boltzmann method, Phys. Rev. E **66**, 026311 (2002).

[16] C. Y. Lim, C. Shu, X. D. Niu, and Y. T. Chew, Application of lattice Boltzmann method to simulate microchannel flows, Phys. Fluids **14**, 2299 (2002).

[17] F. Verhaeghe, L. S. Luo, and B. Blanpain, Lattice Boltzmann modeling of microchannel flow in slip flow regime, J. Comput. Phys. **228**, 147 (2009).

[18] Z. Chai, Z. Guo, L. Zheng, and B. Shi, Lattice Boltzmann simulation of surface roughness effect on gaseous flow in a microchannel, J. Appl. Phys. **104**, 014902 (2008).

[19] G. H. Tang, W. Q. Tao, and Y. L. He, Lattice Boltzmann method for gaseous microflows using kinetic theory boundary conditions, Phys. Fluids **17**, 058101 (2005).

[20] S. Succi, Mesoscopic Modeling of Slip Motion at Fluid-Solid Interfaces with Heterogeneous Catalysis, Phys. Rev. Lett. **89**, 064502 (2002).

[21] L. Szalmás, Slip on curved boundaries in the lattice Boltzmann model, Int. J. Mod. Phys. C **18**, 15 (2007).

[22] L. de L. X. Augusto, J. Ross-Jones, G. C. Lopes, P. Tronville, J. A. S. Gonçalves, M. Rädle, and M. J. Krause, Microfiber filter performance prediction using a lattice Boltzmann method, Commun. Comput. Phys. **23**, 910 (2018).

[23] Z. Guo, B. Shi, and C. Zheng, Velocity inversion of micro cylindrical Couette flow: A lattice Boltzmann study, Comput. Math. Appl. **61**, 3519 (2011).

[24] S. Yuhong, R. W. Barber, and D. R. Emerson, Inverted velocity profiles in rarefied cylindrical Couette gas flow and the impact of the accommodation coefficient, Phys. Fluids **17**, 047102 (2005).

[25] K. Suga, Lattice Boltzmann methods for complex micro-flows: Applicability and limitations for practical Applications, Fluid Dyn. Res. **45**, 034501 (2013).

[26] J. Ren, Q. Zheng, and Y. Li, Curved boundary condition for lattice Boltzmann modeling of binary gaseous micro-scale flows in the slip regime, Phys. A: Stat. Mech. Appl. **550**, 124181 (2020).

[27] S. Tao and Z. Guo, Boundary condition for lattice Boltzmann modeling of microscale gas flows with curved walls in the slip regime, Phys. Rev. E **91**, 043305 (2015).

[28] Z. W. Tian, C. Zou, H. J. Liu, Z. L. Guo, Z. H. Liu, and C. G. Zheng, Lattice Boltzmann scheme for simulating thermal micro-flow, Phys. A: Stat. Mech. Appl. **385**, 59 (2007).

[29] S. Chen and Z. Tian, Simulation of thermal micro-flow using lattice Boltzmann method with Langmuir slip model, Int. J. Heat Fluid Flow **31**, 227 (2010).

[30] G. Silva and V. Semiao, Consistent lattice Boltzmann modeling of low-speed isothermal flows at finite Knudsen numbers in slip-flow regime: Application to plane boundaries, Phys. Rev. E **96**, 013311 (2017).

[31] G. Silva, consistent lattice Boltzmann modeling of low-speed isothermal flows at finite Knudsen numbers in slip-flow regime. II. Application to curved boundaries, Phys. Rev. E **98**, 023302 (2018).

[32] Z. Liu, Z. Mu, and H. Wu, A new curved boundary treatment for LBM modeling of thermal gaseous microflow in the slip regime, Microfluid. Nanofluid. **23**, 27 (2019).

[33] G. Le, O. Oulaid, and J. Zhang, Counter-extrapolation method for conjugate interfaces in computational heat and mass transfer, Phys. Rev. E **91**, 033306 (2015).

[34] L. S. Luo, B. Li, and D. Y. Kwok, Comment on "Discrete Boltzmann Equation for Microfluidics", Phys. Rev. Lett. **92**, 139401 (2004).

[35] P. Lallemand and L. S. Luo, Lattice Boltzmann method for moving boundaries, J. Comput. Phys. **184**, 406 (2003).

[36] G. H. Tang, Y. H. Zhang, and D. R. Emerson, Lattice Boltzmann models for nonequilibrium gas flows, Phys. Rev. E **77**, 046701 (2008).

[37] L. S. Luo, Comment on "Heat transfer and fluid flow in microchannels and nanochannels at high Knudsen number using thermal lattice-Boltzmann method", Phys. Rev. E **84**, 048301 (2011).

[38] P. Lallemand and L. S. Luo, Theory of the lattice Boltzmann method: Dispersion, dissipation, isotropy, Galilean invariance, and stability, Phys. Rev. E **61**, 6546 (2000).

[39] Z. Guo, C. Zheng, and B. Shi, Discrete lattice effects on the forcing term in the lattice Boltzmann method, Phys. Rev. E **65**, 046308 (2002).

[40] C. Cercignani, *The Boltzmann Equation and Its Applications* (Springer-Verlag, New York, 1988).

[41] A. Beskok, G. Em Karniadakis, and W. Trimmer, Rarefaction and compressibility effects in gas microflows, J. Fluids Eng. Trans. ASME **118**, 448 (1996).

[42] R. W. Barber, Y. Sun, X. J. Gu, and D. R. Emerson, Isothermal slip flow over curved surfaces, Vacuum **76**, 73 (2004).

[43] Q. Chen, X. Zhang, and J. Zhang, Improved treatments for general boundary conditions in the lattice Boltzmann method for convection-diffusion and heat transfer processes, Phys. Rev. E **88**, 033304 (2013).

[44] O. Oulaid, Q. Chen, and J. Zhang, Accurate boundary treatments for lattice Boltzmann simulations of electric fields and electro-kinetic applications, J. Phys. A: Math. Theor. **46**, 475501 (2013).

[45] S. Colin, S. G. Kandlikar, S. Garimella, D. Li, and M. R. King, in *Heat Transfer and Fluid Flow in Minichannels and Microchannels* (Elsevier, Oxford, 2006), p. 9.

[46] F. Xie, Y. Li, X. Wang, Y. Wang, G. Lei, and K. Xing, Numerical study on flow and heat transfer characteristics of low pressure gas in slip flow regime, Int. J. Therm. Sci. **124**, 131 (2018).